

Spectral analysis of ASTER data covering part of the Neoproterozoic Allaqi-Heiani suture, Southern Egypt

Fang Qiu ^{a,*}, Mohamed Abdelsalam ^b, Pathik Thakkar ^a

^a Program in Geographic Information Sciences, The University of Texas at Dallas, Richardson, TX 75083-0688, USA

^b Department of Geosciences, The University of Texas at Dallas, Richardson, TX 75083-0688, USA

Received 25 January 2005; received in revised form 31 May 2005; accepted 7 October 2005

Available online 3 January 2006

Abstract

This paper examines the potential of ASTER data in mapping the geology of an arid area in Africa using spectral analysis techniques. Equipped with a relatively broad spectral range, fine spatial resolution, and a large number of bands, ASTER data are especially attractive to many geological researchers in Africa, due to their open availability and associated minimal costs for academic use. The spectral analysis of an ASTER dataset covering part of the Neoproterozoic Allaqi-Heiani suture, Southern Egypt has demonstrated it to be more effective in detecting lithological units than traditional multispectral analysis procedures, such as the maximum likelihood classifier. The effectiveness of these spectral analysis techniques used in this study lies in their ability to compare a pixel spectrum with the spectra of known pure materials, extracted from the spectral endmember selection procedures, including minimum noise factor (MNF), pixel purity index (PPI) and *n*-dimensional visualization. Among the three spectral analysis algorithms employed, spectral angle mapping (SAM) and spectral feature fitting (SFF), produced accurate classifications that were close to the ground reference data. Linear spectral unmixing (LSU), although failing to achieve a satisfactory overall classification accuracy, demonstrated potential in depicting intercalation of layered rocks. It is concluded that these spectral analysis techniques have proven to be useful tools in geological mapping of the arid regions in Africa, with their abilities to capitalize on the enhanced spectral information of ASTER data.

© 2005 Elsevier Ltd. All rights reserved.

Keywords: ASTER data; Spectral analysis; Allaqi-Heiani suture; Geological mapping

1. Introduction

The recent developments in remote sensing technology have witnessed two major trends in sensor improvement. One trend is the refinement of spatial resolution of satellite borne imagery (approximately 1×1 – 4×4 m), characterized by commercial sensor systems such as IKONOS, QuickBird, and OrbView-3. These sensor systems have in mind a target market primarily in urban and suburban applications, where the major data sources had been aerial photographs. The other trend is the enhancement of spectral resolution from a few broad spectral bands, to tens or hundreds of relatively narrow, contiguous and/or non-

contiguous bands. This trend is evidenced by the increasing utilization of various suborbital and satellite imaging spectrometers (i.e., hyperspectral sensor systems), such as airborne visible/infrared imaging spectrometer (AVIRIS), compact airborne spectrographic imager (CASI), and the moderate resolution imager spectrometer (MODIS) on board the NASA's EOS *Terra* and *Aqua* satellites (Jensen, 2000; Zhang et al., 2000). Imaging spectrometry technology is especially welcomed by many earth scientists because it is sensitive to the physical and chemical properties of materials, making it possible to identify the mineral constituents of the surface within the instantaneous-field-of-view (IFOV) (Chabrilat et al., 2000).

The advent of hyperspectral data sets with a large number of bands has pushed the limits of the traditional multispectral classifiers such as maximum likelihood,

* Corresponding author. Tel.: +1 972 883 4134; fax: +1 972 883 2735.
E-mail address: fqiu@utdallas.edu (F. Qiu).

ISODATA, and even artificial neural network approaches (Leica Geosystems, 2003), although their usefulness in hyperspectral data has not been obviated completely. As a result, various spectral analysis techniques have been employed, which make use of the imaging spectroscopy model for approaching hyperspectral data sets. The operation of these techniques often requires the ability to analyze the spectrum of a pixel and compare them with those of pure (i.e., endmember) materials. Some of these techniques were not specifically devised for processing hyperspectral images (Green et al., 1988), and in many respects, are simply an extension of the techniques that were originally used for multispectral data sets. Many other techniques, despite their primary design for use with hyperspectral data, can be applicable logically to multispectral data (Research Systems, Inc., 2002).

As a matter of fact, there is no universal agreement currently on the minimum number of bands beyond which a dataset can be called hyperspectral, although it is often assumed that hyperspectral data should contain at least 10 spectral bands with relatively narrow and often continuous bandwidths in the visible and near infrared (VNIR) spectral regions (Baltavia, 2002). To date, the most widely used hyperspectral data are probably acquired by airborne hyperspectral systems such as AVIRIS (developed by JPL) and HyMap (manufactured by Integrated Spectronics). The value of these datasets lies in its extremely high spectral resolution (for example, AVIRIS has 224 spectral channels, each 10 nm wide, and spanning the electromagnetic region from 400 to 2500 nm) (NASA AVIRIS, 2004), and also in its capability to achieve a possibly very fine spatial resolution when the flight height is arranged sufficiently low. In spite of these advantages, these datasets often incur a relatively high cost per data acquisition mission, having limited availability as with all airborne systems. Therefore, it may not be the ideal choice for many earth science studies in Africa, where economic constraints

are often a concern. Additionally, the geometric distortions present in AVIRIS datasets can sometimes be hard to rectify due to the airborne nature of the sensor. A seemingly possible alternative is the remotely sensed data acquired by satellite borne imaging spectrometers, such as MODIS. Although equipped with a high radiometric capability that collects remotely sensed data in 36 spectral bands, MODIS has coarse spatial resolutions ranging from 250×250 m to 500×500 m and 1×1 km, which have limited its primary use to the monitoring of land ecosystems, and atmospheric and ocean variables at the global level (NASA MODIS, 2004).

The advanced spaceborne thermal emission and reflection radiometer (ASTER) is of special interest to geological remote sensing in that it has a relatively broad spectral range, fine spatial resolution, and a large number of bands among the five sensor systems (i.e., ASTER, CERES, MISR, MODIS, and MOPITT) on board the NASA's *Terra* platform. As shown in Table 1, ASTER is sensitive to emissions in the thermal infrared region, which goes beyond the 2500 nm upper limit of many contemporary hyperspectral sensor systems (Rowan and Mars, 2003). Another advantage of ASTER data is that band 3 (NIR) of the sensor has an additional back-looking telescope that allows the collection of stereoscopic images at 15 m spatial resolution. This along-track stereoscopic capability makes ASTER ideal for geological and geomorphological interpretation (Welch et al., 1998; Yamaguchi et al., 2001; Liu et al., 2004). The most appealing aspect of ASTER data for African geoscientific studies is the open availability of its data, including on-demand standard products for research use at a very low cost (Rowan and Mars, 2003).

While not a typical hyperspectral sensor system, ASTER does provide substantial improvements over the traditional multispectral sensor, such as Landsat thematic mapper (TM), in spatial, spectral and radiometric resolutions. To many researchers, ASTER has become a vital data source

Table 1
ASTER data characteristics compared with those of Landsat TM/ETM+

Region	ASTER				Landsat TM/ETM+			
	Band no.	Spectral (μm)	Spatial (m)	Radiometric	Band no.	Spectral (μm)	Spatial (m)	Radiometric
VNIR	1	0.52–0.60	15	8 bits	1	0.450–0.515	30	8 bits
	2	0.63–0.69			2	0.525–0.605		
	3N	0.78–0.86			3	0.630–0.690		
	3B	0.78–0.86			4	0.750–0.900		
	4	0.78–0.86			Pan.	0.52–0.90		
SWIR	4	1.60–1.70	30	8 bits	5	1.55–1.75	30	
	5	2.145–2.185			7	2.08–2.35		
	6	2.185–2.225						
	7	2.235–2.285						
	8	2.295–2.365						
TIR	9	2.360–2.430	90	12 bits			120/60 (ETM+)	
	10	8.125–8.475						
	11	8.475–8.825						
	12	8.925–9.275						
	13	10.25–10.95			6	10.40–12.50		
	14	10.95–11.65						

for geological mapping because of resolution improvements and the free-of-cost data availability. This is especially true given the possible interrupted availability of Landsat TM/ETM+ sensor data in the future (NASA LANDSAT 7, 2004).

The objective of this paper is to employ spectral image processing techniques that have been used often to process hyperspectral data to analyze ASTER data for the purpose of mapping lithological units in arid regions of Africa, with the hope that these techniques will make effective use of the richer information content furnished by ASTER's relatively high spectral resolution. To this end, we have concentrated our geological study on part of the Neoproterozoic Allaqi-Heiani suture in Southern Egypt. The following section is devoted to introducing the regional setting of the Allaqi-Heiani suture and to the geology of the study area, followed by a description of the ASTER sensor system and the remote sensing dataset used in this research. The spectral image analysis techniques applied to the ASTER dataset are then explained and the results are described. Finally, these results are discussed in terms of their geological implications.

2. The Allaqi-Heiani suture and the geology of the study area

The Allaqi-Heiani suture is a WNW-ESE trending deformation zone in the northern part of the Arabian-Nubian shield defined by a S-verging fold and thrust belt. It is dominated by volcano-sedimentary rocks, dismembered ophiolites, and syn- and post-tectonic granitoids as shown in Fig. 1 (Stern, 1994; Abdelsalam and Stern, 1996; El-Nisr, 1997; Abd El-Naby et al., 2000; El-Kazzaz and Taylor, 2001; Ramadan et al., 2001; Abdelsalam et al., 2003). It is comprised of a 30 km wide zone of highly deformed ophiolitic assemblages, shelf metasediments, arc volcanics and volcanoclastics, and granitoids (Abdelsalam et al., 2003). It extends for more than 250 km from the N-trending Hamisana shear zone in the east to Lake Nasser in the west.

Multispectral remote sensing data have long been employed for geological mapping in arid regions. Several studies have attempted to use the spectral channels from Landsat TM to map the Allaqi-Heiani suture. For example, Ramadan et al. (2001) used Landsat TM images to map gold-bearing massive sulfide deposits in the western part of the Allaqi-Heiani suture. Kusky and Ramadan

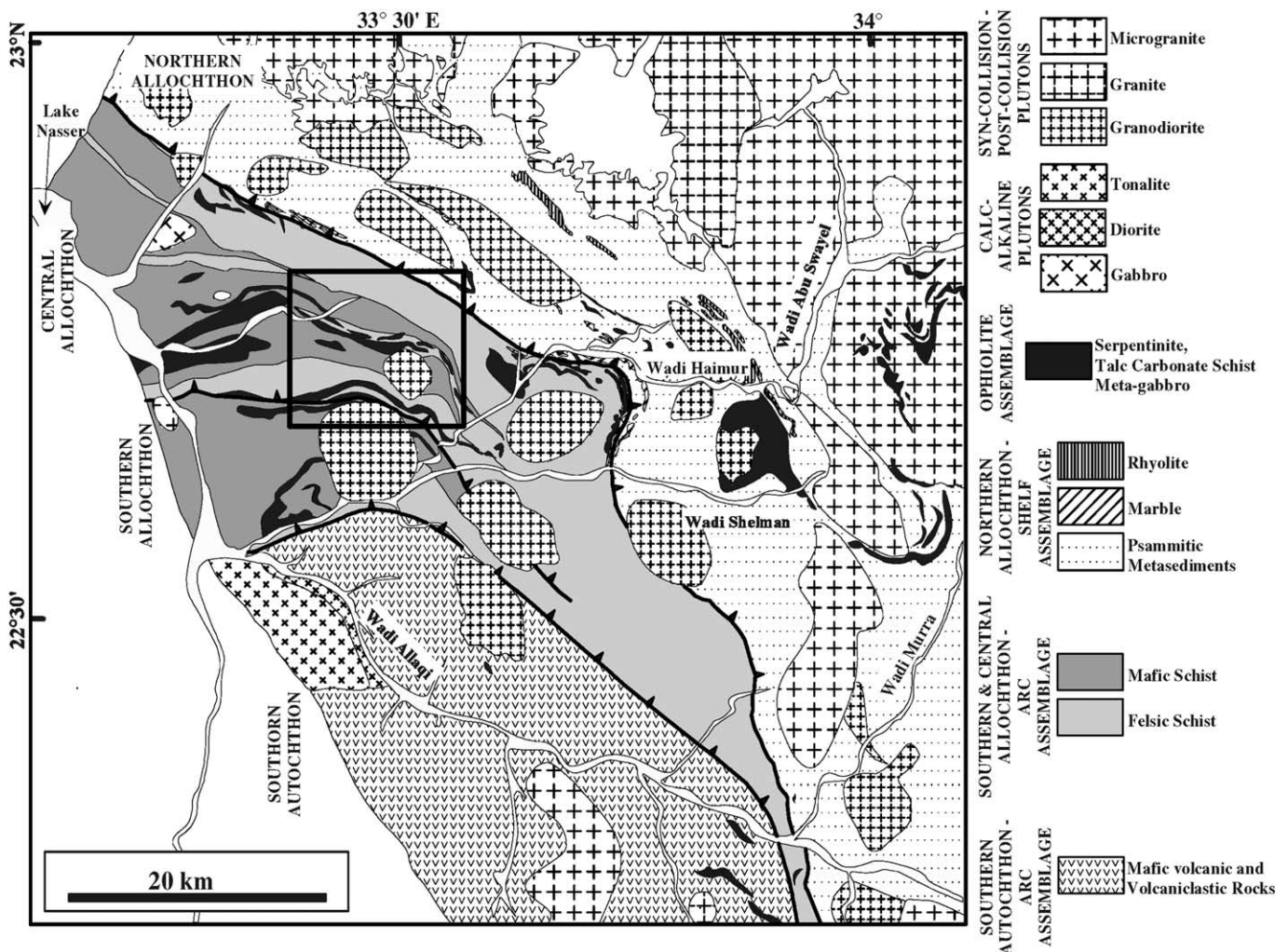


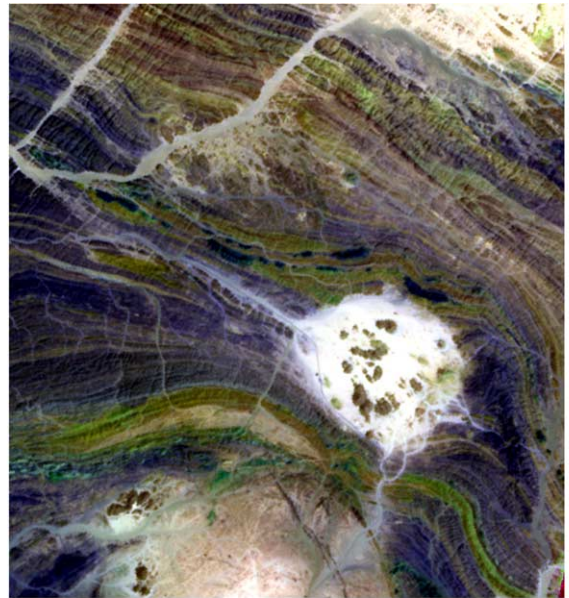
Fig. 1. The general geology map in the study area covering the Allaqi-Heiani suture, Southern Egypt (modify after Abdelsalam et al., 2003).

(2002) used Landsat TM images to remotely sense structures and their controls on mineralization in the western part of the suture.

This study focused on the Western Allaqi-Heiani suture because its lithological variation provides an excellent opportunity for examining the usefulness of spectral analysis of ASTER data for geological mapping in arid regions. We have collected ample in situ geological information that can be used to verify the remote sensing investigation. To this end, we selected a 10×10 km study area (as shown within the black box in Fig. 1) with low-lying relief and dominantly WNW-ESE trending ridges that follow the regional foliation of the layered volcano-sedimentary rocks and ophiolite assemblages. These ridges are sometimes interrupted by isolated low-lying hills and peaks of granitic bodies. This study area occupies part of a S-verging fold and thrust belt comprising a northern allochthon, a central allochthon, and a southern autochthon (Abdelsalam et al., 2003). It falls within the central allochthon and is dominated by the following rock types: (1) volcano-sedimentary rocks; (2) ophiolitic rocks; (3) granitic intrusions; (4) quaternary sediments, dominantly sand; and (5) wadi fill. The volcano-sedimentary rocks are primarily made-up of amphibole and quartzo-feldspathic schists, which might have been of mafic volcanic origin, and psammitic and felsic volcanic origins, respectively. These are mainly schistose with a WNW-ESE regional foliation. The ophiolitic rocks comprise serpentinites, talc- and talc-carbonate schist, and gabbros. Similar to the volcano-sedimentary rocks, the ophiolites are mostly deformed by WNW-ESE trending foliation. The granitic intrusions form circular bodies that cross-cut the regional foliation. These are largely granitic in composition and they are either not foliated or weakly foliated. The quaternary sediments are dominantly sands derived from the weathering of the granitic bodies, although these are sometimes mixed with weathered products of other rock types.

3. The ASTER remote sensing data

The ASTER data used in this study are cloud free level 1B data acquired on April 06, 2001. The image has been pre-georeferenced to UTM Zone 14 North projection with WGS-84 datum. The ASTER image was then resampled so that all 14 bands have the same 15×15 m pixel size and then clipped to the study area. The color display of the ASTER data (R, G, B = Band 7, 4, 3) covering the area is shown in Fig. 2a. The drape of the image (R, G, B = Band 3, 2, 1) on top of a digital elevation model (DEM) derived from the ASTER band 3 stereoscopic data is shown in Fig. 2b. ASTER DEMs can be ordered online from NASA as a higher level product. ASTER DEMs can also be extracted with specialized software such as AsterDTM (SulSoft Ltda., 2004), as used in this study. However, the ASTER DEM is not incorporated in the subsequent analysis as ancillary data because it did not help to improve the classification.



(a)



(b)

Fig. 2. (a) The color display of the ASTER data (R, G, B = Band 7, 4, 3) covering the study area. (b) The image draped (R, G, B = Band 3, 2, 1) on top of a digital elevation model (DEM) derived from the ASTER band 3 stereoscopic data.

A comparison between ASTER and Landsat TM/ETM+ sensor characteristics (Table 1) demonstrates that ASTER's spectral, spatial and radiometric resolutions are endowed with substantial improvements over traditional multispectral datasets. One of the spectral enhancements in ASTER occurs in the TIR region, which bears a significant implication in mapping surface materials and lithological units, when important rock-forming minerals do not exhibit absorption features in the VNIR and SWIR regions (Rowan and Mars, 2003; Vaughan et al., 2003). To capitalize on this improved spectral information, this study applies various spectral analysis techniques to the ASTER dataset in an attempt to identify the most appropriate algorithm(s) to be used with ASTER imagery in mapping geological units.

4. Remote sensing analysis and results

Many commonly used spectral image analysis techniques are based on the fact that remotely sensed imagery is sampled with numerous spectral bands at narrow bandwidths

(often on the order of tens of nanometers), making it possible to construct a spectrum for each pixel in the image. The spectrum can then be compared with the spectra of known pure materials such as minerals, vegetation, and atmospheric gases. These pure materials are often referred to as endmembers. The spectra of the endmembers primarily come from three different sources including (1) image derived “pure pixels”; (2) in situ spectroradiometric measurement; and (3) laboratory based spectral libraries such as those provided by Johns Hopkins University, the US Geological Survey, and NASA’s Jet Propulsion Laboratory (ASTER Spectral Library, 2004). The use of in situ measurements and the laboratory-based library often require the removal of atmospheric and topographic attenuation from the remotely sensed image (Jensen, 2005). The existence of possible vertical scaling anomalies in ASTER data and SWIR crosstalk from band 5 and band 9 makes the data difficult to use for spectral analysis based on direct comparisons with library or field spectra (NASA ASTER, 2004). Conducting further rigorous radiometric corrections to the ASTER data in order to obtain surface reflectance and radiance is also not feasible because the information about the atmospheric properties above the study area at the time the ASTER data were collected (such as barometric pressure, relative humidity, and visibility) are not available. Therefore, we have employed the endmembers derived from the image using pixel purity index and n -dimensional visualization procedures for the subsequent analyses.

To effectively extract endmembers from high dimensional remote sensing data and to effectively process the data, it is often necessary that the dimensionality of the original data be decreased and noise in the data be segregated first, so the visualizing complexity and computational requirement for the subsequent analyses can be reduced. This is often achieved through applying a minimum noise fraction (MNF) transform to the high dimensional data. Once the inherent dimensionality of the image data is determined using the MNF transform, endmembers can then be derived by using PPI and n -dimensional visualization techniques from the higher-order MNF eigenimages. These endmembers can be compared subsequently with the remote sensing data to determine the surface materials of each pixel by employing one of the spectral analysis algorithms, such as spectral angle mapper (SAM), spectral feature fitting (SFF), or linear spectral unmixing (LSU). The methodology of the spectral image analysis techniques applied to the ASTER data are explained below. The results from these techniques are described and compared with each other, and with those obtained from traditional multispectral image classification techniques, such as maximum likelihood classification.

4.1. Minimum noise fraction (MNF) transform

The MNF transform is composed of two consecutive principal component (PC) transforms (Green et al., 1988). The first PC transform focuses on whitening noise

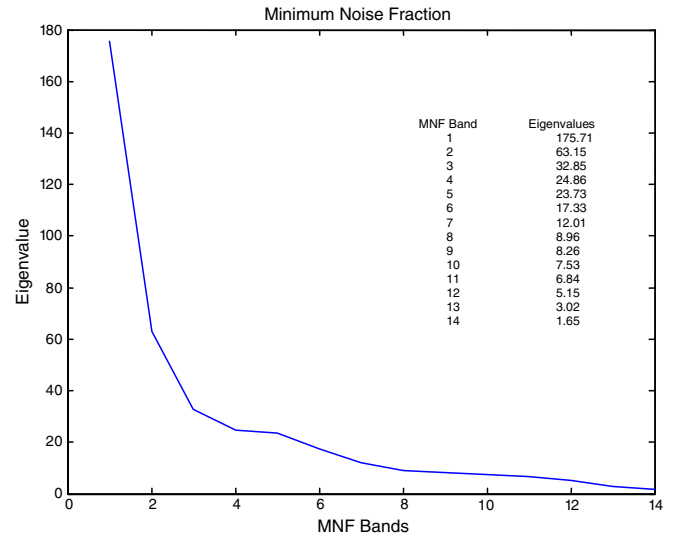


Fig. 3. The MNF eigenvalues plot of the 14 eigenimages of the ASTER data.

by decorrelating and rescaling the noise in the data, producing data in which the noise has unit variance and no band-to-band correlations. The transformed noise-whitened data are then subjected to a second standard PC transform, giving rise to final outputs that are not correlated and are arranged in terms of decreasing information content (Research Systems, Inc., 2002). The eigenvalues of the 14 output MNF eigenimages of the ASTER data are displayed in Fig. 3.

In a common practice, MNF components with eigenvalues less than 1 are usually excluded from the data as noise in order to improve the subsequent spectral processing results, since eigenimages with near-unity eigenvalues are normally noise-dominated (Jensen, 2005). However, Fig. 3 shows that all the eigenvalues of the transformed ASTER data are greater than 1, although the actual value does drop off with increasing component order. Consequently, all the 14 bands of the ASTER data were retained for subsequent data processing. The dimensionality of the data, however, is still very manageable compared to most hyperspectral analyses.

The MNF transform applied to the ASTER data achieved a reasonable separation of coherent signal from complementary noise, therefore the MNF transformed eigenimages were employed and coupled with pixel purity index and n -dimensional visualization techniques to facilitate the extraction of the endmembers. As in many studies, decorrelation and scaling of the noise in the MNF transform provide good insight into the relationship between different endmembers of the image and their spatial distribution of coherency.

4.2. Pixel purity index

Identifying endmember pixels whose spectra are extreme (or spectrally pure) is not a simple task, especially in

high-dimension image datasets. This is because most pixels often contain varying proportions of different materials of more than one type. Unlike training sites in multispectral data, which are usually arithmetic mean spectral vectors that can be selected easily manually or with regional growth tools (Jensen, 2005), the extraction of endmembers often has to be based on rigorous mathematical algorithms, such as pixel purity index.

Pixel purity index (PPI) is a means to determine automatically the relative purity of the pixels from the higher-order MNF eigenimages using the convex geometry argument (Boardman, 1993; Boardman et al., 1995). By repeatedly projecting n -dimensional scatter plots of the MNF images onto a random unit vector, a PPI image is formed in which the digital number (DN) of each pixel corresponds to the total number of times that the pixel was judged as “extreme” (i.e., falling onto the ends of the unit vector) in all projections. Typically, the brighter the pixel in the PPI image the higher the relative purity because it was more frequently recorded as being a spectrally extreme pixel. To reduce the number of pixels to be analyzed for endmember determination and to facilitate the separation of purer materials from mixed, a 10,000-projection of the scatter plot and a threshold factor of 2.5 is applied to the PPI image to select the most pure PPI pixels.

4.3. n -Dimensional endmember visualization

After applying PPI thresholding, the data volume to be analyzed has been effectively reduced. However, it is still possible that many less “pure” pixels have crept in as candidate endmembers during the automatic selection process. To further refine the selection of the most spectrally pure endmembers from the derived two-dimensional PPI image and more importantly, to label them with specific endmember types (i.e., to assign these endmembers to specific rock types), it is essential to reexamine visually the selected pixels in the n -dimensional feature space and to assign them manually to appropriate types (Boardman, 1993; Boardman and Kruse, 1994). This is accomplished by using two or more MNF eigenimages to form a n -dimensional scatter plot. All the pixels that were previously selected using the PPI thresholding procedure are displayed as pixel clouds in the n -dimensional spectral space. To make possible the visualization of a scatter plot with more than two dimensions, the pixel clouds of high dimensions are cast on the two-dimensional display screen. With interactive rotation and visualization by an image analyst in the spectral space, the convex corners of the pixel clouds can be located and designated as the purest spectral endmembers. As a result, the number of endmembers to be analyzed is further reduced. The actual spatial locations of these final spectral endmembers are then determined in the two-dimensional image space of the MNF or the original dataset, and they are labeled with the specific endmember types for these locations.

The pixel values of all the 14 MNF eigenimages are used to form a display of the n -dimensional visualization projec-

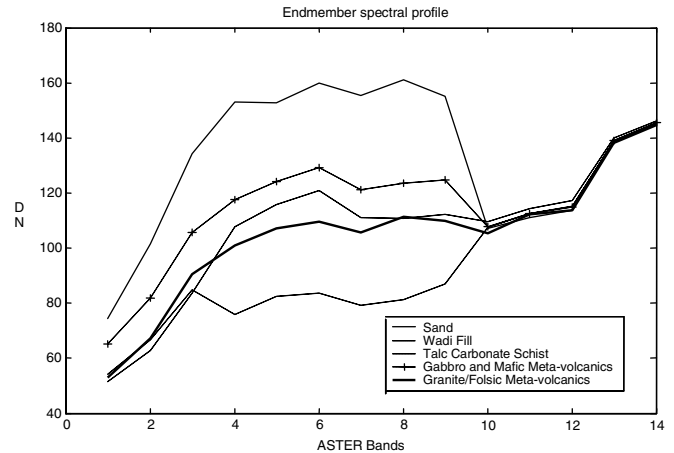


Fig. 4. The spectral profile of the endmembers presented relative to ASTER band number.

tion of the PPI thresholded pixels. Any number of combinations of bands may be displayed to create the n -dimensional feature plot (e.g., a combination of only two or three coherent MNF eigenimages produces a two- or three-dimensional scatter plot). However, to enable the interactive and automatic random rotation of the axes, at least three bands must be selected. During rotation, groups of pixels at the corners of the rotating scatter plot that can be isolated from other data clouds will be chosen as different endmembers that correspond to specific rock types. With reference to their actual locations in the image space, these different types of endmembers are then labeled with the appropriate rock types and highlighted with different colors. The mean spectra (reflectance values) of all endmember groups or the spectra of individual endmembers are then derived from the original images based on their spatial location.

For the ASTER dataset covering the study area, five major types of endmembers including sand, gabbro and mafic meta-volcanic rocks, talc-carbonate schist, wadi fill, and granite and felsic meta-volcanic rocks were extracted. The profile of the spectral characteristics of these endmembers is presented relative to the band numbers in Fig. 4. The five image spectra derived from the n -dimensional endmember visualization procedure are used as reference spectra for subsequent spectral image analysis. In general, the overall shapes of the spectral curves of the reference endmembers are similar. However, they can be distinguished easily from one another based on the differences in both the angles of the curves and the magnitude of digital number. The difference in digital number between the extracted endmembers is more significant though, especially in the VNIR and SWIR bands (Fig. 4).

4.4. Spectral angle mapper

In order to extract thematic information from the ASTER image it is often necessary to compare individually

each unclassified pixel of the image with the image-derived reference spectra and then determine which reference spectrum most closely resembles the spectral characteristics of the pixel. Spectral angle mapper (SAM) is a procedure that determines the similarity between a pixel and each of the reference spectra based on the calculation of the “spectral angle” between them (Kruse et al., 1993). Both the pixel and reference spectra are considered as vectors in the feature space with its dimensionality (n) equal to the number of bands. The “angular distance” between a reference spectrum vector (t) and the unknown pixel measurement vector (r) in n -dimensional space is computed using the following equation (Research Systems, Inc., 2002):

$$\alpha = \cos^{-1} \left(\frac{\sum_{i=1}^n t_i r_i}{\left(\sum_{i=1}^n t_i^2\right)^{\frac{1}{2}} \left(\sum_{i=1}^n r_i^2\right)^{\frac{1}{2}}} \right)$$

For each reference spectrum (r) chosen as endmember, one output image is created with every pixel containing a value representing the spectral angle (α) between the pixel

(t) and that specific reference spectrum. The resulting spectral angle maps form a brand new SAM image cube with the dimension equal to the number of reference spectra (five in this case). Within an image for a specific reference spectrum the pixels with a smaller spectral angle appear darker, standing for a close resemblance to that reference spectrum (Research Systems, Inc., 2002; Jensen, 2005). To convert the SAM image cube into a classification map, each pixel is assigned to the reference spectrum class that yields the closest match (Kruse et al., 1993; Boardman and Kruse, 1994). Fig. 5a displays the final classification map derived from the SAM analysis procedure being applied to the original ASTER dataset. Pixels for sand are assigned to red, gabbros and mafic meta-volcanic rocks to green, talc-carbonate schist to blue, wadi fill to cyan, and granites and felsic meta-volcanic rocks to yellow. Reference sites with a total of 267 points are collected from visual image interpretation coupled with in situ verification. Table 2a shows the accuracy assessment matrix of the SAM analysis results based on the 267 reference sites. In addition to

Table 2
Accuracy assessment matrices for the four different classification methods used in the study

	Sand	Gabbro	Talc	Granite	Wadi fill	Total	Percent
<i>(a) Classification accuracy assessment for the spectral angle mapper (SAM) approach</i>							
SAM							
Sand	30	0	0	7	0	37	81.08
Gabbro	0	34	9	2	23	68	50.00
Talc	0	0	48	0	0	48	100.00
Granite	0	4	0	52	2	58	89.66
Wadi fill	0	11	2	2	41	56	73.21
Total	30	49	59	63	66	267	
Percent	100.00	69.39	81.36	82.54	62.12		76.78
<i>(b) Classification accuracy assessment for the spectral feature fitting (SFF) approach</i>							
SFF							
Sand	27	2	0	3	0	32	84.38
Gabbro	0	33	0	9	1	43	76.74
Talc	0	5	43	0	4	52	82.69
Granite	3	1	0	43	0	47	91.49
Wadi fill	0	8	16	8	61	93	65.59
Total	30	49	59	63	66	267	
Percent	90.00	67.35	72.88	68.25	92.42		77.53
<i>(c) Classification accuracy assessment for the linear spectral unmixing (LSU) approach</i>							
LSU							
Sand	30	1	0	18	3	52	57.69
Gabbro	0	37	4	8	22	71	52.11
Talc	0	10	51	3	28	92	55.43
Granite	0	1	2	33	6	42	78.57
Wadi fill	0	0	2	1	7	10	70.00
Total	30	49	59	63	66	267	
Percent	100.00	75.51	86.44	52.38	10.61		59.18
<i>(d) Classification accuracy assessment for the maximum likelihood classification (MLC) approach</i>							
MLC							
Sand	30	13	3	16	23	85	35.29
Gabbro	0	1	0	0	0	1	100.00
Talc	0	7	50	0	7	64	78.13
Granite	0	28	6	47	36	117	40.17
Wadi fill	0	0	0	0	0	0	0.00
Total	30	49	59	63	66	267	
Percent	100.00	2.04	84.75	74.60	0.00		47.94

total classification accuracy, detailed producer and user's accuracies characterizing measure of omission and commission error, respectively, are also reported in all the accuracy assessment tables.

SAM based classification has been impressively accurate in mapping the talc-carbonate schist (with a very high user's accuracy of 100% and a producer's accuracy of 81.36%), especially for the small bodies that occur in the central part of the images enclosed within the NW-trending belt of mafic meta-volcanic rocks. The classification is also effective in identifying sand in general (with a very high producer's accuracy of 100% and a user's accuracy of 81.08%). Particularly it shows the circular body in the central part of the image as dominated by sand, which has resulted from the weathering of what was once a granitic mass, the remnants of which are now preserved as isolated outcrops within the circular structure. In addition, the classification clearly shows two bands of gabbroic bodies trending WNW and enclosing a crescent-shaped granitic body. However, the gabbro and mafic meta-volcanics have to some extent been overestimated with a user's accuracy around 50%.

4.5. Spectral feature fitting

Primarily used for geologic applications, spectral feature fitting (SFF) is an attempt to directly identify a material by fitting unknown image spectra to reference spectra (Clark and Roush, 1984; Clark et al., 1990, 1991, 1992; Crowley and Clark, 1992; Clark and Swayze, 1995; Swayze and Clark, 1995). The reference spectra can be extracted either from the image-derived endmembers or from a spectral library. As an absorption-feature-based method, both the reference and unknown spectra should have the continuum (background reflectance) removed (Clark and Roush, 1984; Crowley and Clark, 1992; Swayze and Clark, 1995). The fitting of the image spectra to reference spectra is accomplished through two-step spectral matching procedures including image scaling and least-squares-fit. The first step involves scaling each reference endmember spectrum to match the unknown spectrum. For every reference spectrum, a "scale" image is created by first subtracting the continuum-removed-spectra from one, thus inverting them and making the continuum zero. A single multiplicative scaling factor is then determined for the reference spectrum to match the unknown spectrum. The second step is based on the computation of the least-squares-fit between each reference endmember and the unknown spectrum on a band-by-band basis. The total root-mean-square (RMS) error derived from the least-square-fit is then used to form an error image for each reference endmember. For each reference spectrum a "fitting" image is then created based on the ratio of scale/RMS images indicating how well each unknown pixel spectrum resembles a reference spectrum (Research Systems, Inc., 2002). The higher the pixel values in the "fit" image, the better the matching of the corresponding pixels to a reference spectrum. The final

classification image derived from SFF is displayed in Fig. 5b showing the five classes with the same color scheme and its corresponding accuracy assessment matrix is given in Table 2b.

Similar to the SAM image the SFF image is very successful in showing the geographic extent of sand covered regions (with a producer's accuracy of 90% and a user's accuracy of 84.38%), demonstrated especially by the circular body in the middle of the image. In addition, the SFF image is more effective than the SAM image in refining the extent of the regions covered with gabbros and mafic meta-volcanics (76.74% for SFF vs. 50% for SAM in user's accuracy). For example, the relationship between the gabbro bands and the crescent-shaped granitic body is better defined in this image than the SAM image. However, this method is less effective in showing the actual extent of the talc-carbonate schist than SAM (82.69% for SFF vs. 100% for SAM in user's accuracy). This classification shows more talc-carbonate schist in the NW and SE parts of the image than the reference data indicate. Moreover, it fails to show the small talc-carbonate bodies that are present in the central part of the image.

4.6. Linear spectral unmixing (LSU)

Linear spectral unmixing (LSU), also known as sub-pixel sampling, or spectral mixture analysis, is a widely used procedure to determine the proportion of constituent materials within a pixel based on the materials' spectral characteristics (Boardman, 1989, 1992). In a geological environment most of the pixels of an image are not pure. A pixel value is often a mixture of the energy reflected or emitted from different materials within IFOV. However, most classification procedures only report the class of the dominant constituent of the pixel. Using sub-pixel sampling classification, on the other hand, each unknown pixel spectrum is represented as a combination of a finite number of spectrally distinct materials. As a result the abundance of each pure endmember class within the pixel is informed (Jensen, 2005). A linear combination model is often assumed to determine the relative contributions of the different spectral components present in the image, although it is acknowledged that some non-linear behavior due to microscopic scale mixing occurs (Chabrilat et al., 2000).

With all of the theoretically pure endmembers identified in the image, the linear spectral unmixing is solved for each unknown pixel spectra and produces a cube of fraction images of each endmember. The fractions for each pixel of all derived images are positive and depict a sub-pixel estimate of the relative abundance for the corresponding endmember at that pixel and all these fractions will sum to 1 (Adams et al., 1995). It is also possible to produce a standard-deviation image or a root-mean-square (RMS) error image, revealing the units that are not satisfactorily explained by the proposed model. The fraction image cube can be similarly collapsed into a hardened classification

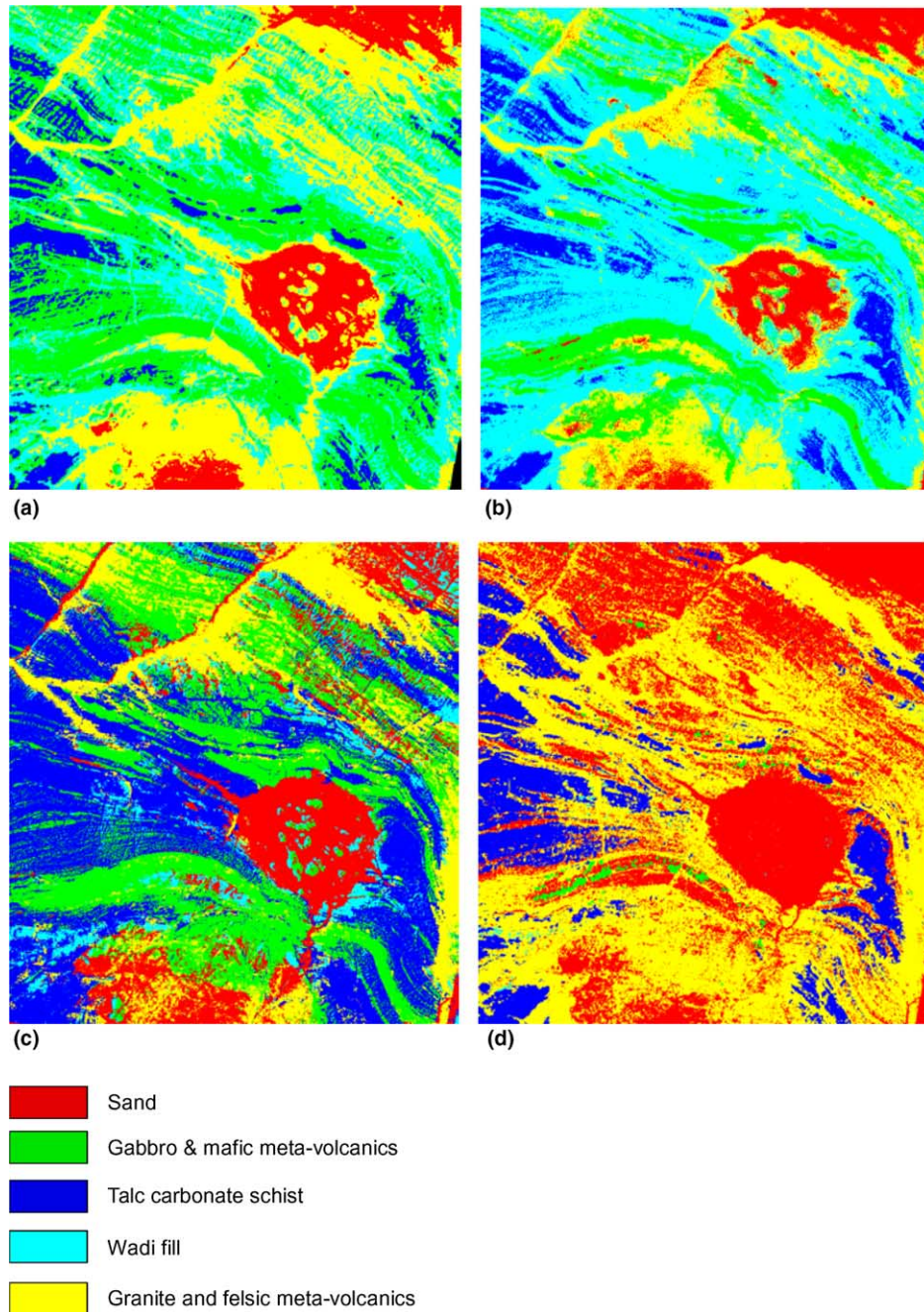


Fig. 5. Final classification image maps for (a) spectral angle mapper (b) spectral feature fitting, (c) linear spectral unmixing, (d) maximum likelihood classifier.

map by assigning each pixel to the class of the dominant endmember.

Fig. 5c is the final classification image derived from LSU analysis procedure and Table 2c is the corresponding error matrix. This image is superior over the SAM and SFF images in its ability to indicate accurately the nature of intercalation between different materials, especially in the layered rocks represented by the meta-volcanic rocks and the talc-carbonate schist and gabbros. However, this classification has assigned a greater portion of the image to talc-carbonate schist (with a user's accuracy of 55.43%), far

removed from what the reference data suggest. Sand and gabbros and mafic meta-volcanics are also overestimated (with user accuracies of 57.69% and 52.11%, respectively). This may be caused by misclassification of Wadi fill to other classes, evidenced by its high omission error (i.e., 10.61% for Wadi fill in producer's accuracy).

Compared with results obtained from the spectral analysis procedures, the traditional multispectral image classification method (i.e., maximum likelihood) is less effective in the identification of different lithological units (Fig. 5d), as evidenced by a very low total classification accuracy of

47.94% (Table 2d). The spatial distribution detail of the different rock types is completely missing in the maximum likelihood classification. Much of the study area has been classified as either sand or granitic and felsic meta-volcanic rocks (with producer's accuracies of 35.29% and 40.17%, respectively). The only relatively accurate classification is the talc-carbonate (with a producer's accuracy of 84.75% and a user's accuracy of 78.13%), especially for the small bodies in the central part of the image. This might be due to the very distinctive spectral characteristics of these rocks compared to the surrounding rock types. However, even in the case of such distinctive lithology the talc-carbonate schist has been somewhat over-estimated especially in the western part of the study area.

5. Discussion

In general, not one spectral analysis procedure is consistently superior to others judged by the comparison of our analysis results with the reference data. Each of the three hyperspectral classification techniques has its unique strengths and limitations. The spectral analysis method based on LSU has a relative advantage in terms of better definition of the intercalation nature of layered rocks. However, in terms of overall classification accuracy, SAM and SFF procedures seem to yield classification results closer to the reference data, with total accuracies of 76.78% and 77.53%, respectively.

SAM classifies most of the rock types used as endmembers accurately, with the exception of only gabbro and mafic meta-volcanic rocks. SAM also reveals many important details of various lithological units such as the small lessees of talc-carbonate schist within the mafic metavolcanic rocks. The advantage of SAM is attributed to the fact that SAM determines the similarity of two spectra based on calculating the "spectral angle" between them. As long as the angles or directions of the spectral vectors, which determine the "color" of materials, are different, SAM can differentiate them. The spectral angles of sand and talc-carbonate schist are quite distinctive compared with the other three types in the spectral profile (Fig. 4). Therefore, it is not a surprise that SAM is very effective in differentiating sand and talc-carbonate schist from other materials. However, given that only the angles or "direction" of the spectra vector is taken into consideration and the magnitude of reflectance or "length" of the vector is ignored, SAM is insensitive to the unknown reflectance gain factor (Research Systems, Inc., 2002). Since the "length" of a spectral vector is related to the fullness of the illumination a pixel receives, as long as the colors of the materials are similar all possible illuminations are treated equally in SAM. This explains why gabbro and mafic meta-volcanic rocks are confused with wadi fill in the SAM based classification. For example, 11 out of 49 reference points for gabbro were misclassified as Wadi fill, and 23 out of 66 reference points for wadi fill were misclassified as gabbro (Table 2a). These two materials have a close similarity

in the spectrum "direction", although they are still separable based on the spectral "length" (Fig. 4).

SFF demonstrates better effectiveness in mapping the extent of the regions covered with gabbros and mafic meta-volcanic rocks than SAM. It has proven to achieve the best balance of classification accuracy among different rock types probably due to the fact that SFF is primarily reliant on the spectral "length" of the spectrum vectors, which are relatively more distinguishable in the spectral profile of the endmembers (Fig. 4). The weakness of SFF is that it expects image data to be reduced to surface reflectance or emissivity. The continuum corresponding to a background signal unrelated to specific absorption features of interest should be removed from the reflectance and the separation of temperature from emissivity data prior to analysis are also expected (Clark and Roush, 1984; Green and Craig, 1985; Kruse et al., 1985). Failing to do so due to the lack of atmospheric property information may have caused the misclassification of certain rock types. For example, the talc-carbonate schist is not separable from the surrounding wadi fill with 16 out of 59 reference points for talc-carbonate schist misclassified as wadi fill.

LSU classification has the advantage over other procedures in showing the intercalation nature of the layered meta-volcanic rocks. However, the LSU classification result in general is unacceptable with a total accuracy of only 59.18%. This may be ascribed to the fact that LSU assumes we have identified all of the theoretically pure classes (endmembers) in the image data such that their proportions will sum to 1 at each pixel. While the identified endmembers are the purest pixels relative to all others in the image, in reality, it is still likely that albedo contributions from other materials are present in the pixels (for example, soil background reflectance). Even if the pixels extracted are spectrally pure many scientists find it difficult to identify all possible constituent endmembers in each pixel of the image (Jensen, 2005). An additional explanation could be the existence of possible non-linear combinations in the pixels of the image and the high correlation of the ASTER SWIR bands, which has violated another assumption of the LSU algorithm (Chabrilat et al., 2000).

Compared with traditional multispectral classification procedures, however, all the spectral analysis techniques used here have exhibited greater effectiveness in classifying the ASTER data for the purpose of geological mapping in arid regions. This is probably because maximum likelihood classifier has to rely on mean spectrum vectors associated with the training sites, rather than the extreme spectra of the pure endmembers derived from PPI and *n*-visualization procedures. As a result, it is unable to take advantage of the rich spectral information provided by ASTER data.

6. Summary and conclusions

This paper has investigated the usage of ASTER data for mapping the geology of an arid area in Africa. As

one of the recent developments in remote sensing technology, ASTER data provide not only improved spatial and radiometric resolutions, but also much richer spectral information content when compared with traditional multiple spectral remote sensing data such as Landsat TM/ETM+. The open availability of ASTER data with an associated minimal cost makes it a very attractive choice for many earth science researchers in Africa.

ASTER data covering part of the Neoproterozoic Allaqi-Heiani suture, Southern Egypt were analyzed using several spectral image processing techniques, which have demonstrated their potential in estimating lithological units through a better use of the enhanced spectral characteristics of the ASTER data.

The spectral analysis techniques employed were implemented based on the comparison of a pixel spectrum with the spectra of known pure materials, which can be effectively extracted using endmember selection procedures such as minimum noise factor (MNF), pixel purity index (PPI) and *n*-dimensional visualization.

Three spectral analysis procedures, including spectral angle mapper (SAM), spectral feature fitting (SFF) and linear spectral unmixing (LSU), were applied to the ASTER data. They resulted in better classification accuracies than multispectral classifier, such as the maximum likelihood classifier. Although LSU exhibits potential in depicting intercalation of layered rocks it fails to achieve a satisfactory overall classification accuracy, possibly due to the violation of the two LSU key assumptions: the linearity of mixture model, and the purity and completeness of spectral endmembers. SAM and SFF, which examine the differences in either spectral angle or reflectance magnitude of the spectrum, produced accurate classifications that were sufficiently close to the reference data. In spite of some limitations, SAM and SFF proved to be effective techniques in mapping lithological units in an arid area and their results can be improved further if data calibration can be applied with the support of atmospheric information.

SAM demonstrated strength in mapping distribution detail for lithological units, while SFF was good at achieving the best balance of classification accuracy among different rock types. It is envisioned that a new spectral analysis technique, which makes use of both the spectral angle and the reflectance magnitude information of the spectrum, will be able to produce an improved classification. By bringing together the strengths of both SAM and SFF, while avoiding their respective shortcomings, a superior technique should ensue. The development of such a technique thus will be one of our major future academic pursuits.

Acknowledgments

The authors like to extend our appreciation to Drs. Ronald Briggs, Michaela Frei, R. Richter DLR, Oberpfaffenhofen, Ms. Annie Hsu, Mrs. Shari Liu and one anonymous reviewer for reviewing the manuscript. We also want to acknowledge Jian Huang, Sherif M.

Elnagdy and Dianwei Ren for their help with part of the research work.

References

- Abd El-Naby, H., Frisch, W., Hegner, E., 2000. Evolution of the Pan-African Wadi Haimur metamorphic sole, Eastern Desert, Egypt. *Journal of Metamorphic Petrology* 18.
- Abdelsalam, M.G., Stern, R.J., 1996. Sutures and shear zones in the Arabian-Nubian Shield. *Journal of African Earth Sciences* 23.
- Abdelsalam, M.G., Abdeen, M.M., Dwaidar, H.M., Stern, R.J., 2003. Structural evolution of the Neoproterozoic Western Allaqi-Heiani suture, Southern Egypt. *Precambrian Research* 124, 87–104.
- Adams, J.B., Sabot, D.E., Kapos, V., Almeida, F., Roberts, D.A., Smith, M.O., Gillespie, A.R., 1995. Classification of multispectral images based on fractions of endmembers: application to land cover change in the Brazilian Amazon. *Remote Sensing of Environment* 52, 137–154.
- ASTER Spectral Library, 2004. Contains the Johns Hopkins University Spectral Library, Jet Propulsion Laboratory Spectral Library, and the U.S. Geological Survey Spectral Library. Available from: <<http://speclab.jpl.nasa.gov>>.
- Baltsavia, E.P., 2002. Special section on image spectroscopy and hyperspectral imaging. *ISPRS Journal of Photogrammetry and Remote Sensing* 57, 169–170.
- Boardman, J.W., 1989. Inversion of imaging spectrometry data using singular value decomposition. In: *IGARSS'89, 12th Canadian Symposium on Remote Sensing*, pp. 2069–2072.
- Boardman, J.W., 1992. Sedimentary facies analysis using imaging spectrometry: a geophysical inverse problem. Unpublished Ph.D. thesis, University of Colorado.
- Boardman, J.W., 1993. Automating spectral unmixing of AVIRIS data using convex geometry concepts. In: *Summaries of the 4th Annual JPL Air-borne Geoscience Workshop, Pasadena*, pp. 11–14.
- Boardman, J.W., Kruse, F.A., 1994. Automatic spectral analysis: a geological example using AVIRIS data, North Grapevine Mountain, Nevada. In: *10th Thematic Conference on Geologic Remote Sensing, Ann Arbor*, pp. 407–418.
- Boardman, J.W., Kruse, F.A., Green, R.O., 1995. Mapping target signatures via partial unmixing of AVIRIS data. In: *Summaries, Fifth JPL Airborne Earth Science Workshop*, pp. 23–26.
- Chabrilat, S., Pinet, P.C., Ceuleneer, G., Johnson, P.E., Mustard, J.F., 2000. Ronda peridotite massif: methodology for its geological mapping and lithological discrimination from airborne hyperspectral data. *International Journal of Remote Sensing* 21, 2363–2388.
- Clark, R.N., Roush, T.L., 1984. Reflectance spectroscopy: quantitative analysis techniques for remote sensing applications. *Journal of Geophysical Research* 89, 6329–6340.
- Clark, R.N., Swayze, G.A., 1995. Mapping minerals, amorphous materials, environmental materials, vegetation, water, ice, and snow, and other materials. In: *The USGS Tricorder Algorithm, Summaries of the Fifth Annual JPL Airborne Earth Science Workshop*, pp. 39–40.
- Clark, R.N., Gallagher, A.J., Swayze, G.A., 1990. Material absorption band depth mapping of imaging spectrometer data using the complete band shape least squares algorithm simultaneously fit to multiple spectral features from multiple materials. In: *Proceedings of the Third Airborne Visible/Infrared Imaging Spectrometer (AVIRIS) Workshop*, pp. 176–186.
- Clark, R.N., Swayze, G.A., Gallagher, A., 1992. Mapping the mineralogy and lithology of Canyonlands, Utah with imaging spectrometer data and the multiple spectral feature mapping algorithm. In: *Summaries of the Third Annual JPL Airborne Geoscience Workshop*, pp. 11–13.
- Clark, R.N., Swayze, G.A., Gallagher, A., Gorelick, N., Kruse, F.A., 1991. Mapping with imaging spectrometer data using the complete band shape least-squares algorithm simultaneously fit to multiple spectral features from multiple materials. In: *Proceedings, 3rd*

- Airborne Visible/Infrared Imaging Spectrometer (AVIRIS) Workshop, pp. 2–3.
- Crowley, J.K., Clark, R.N., 1992. AVIRIS study of Death Valley evaporite deposits using least-squares band-fitting methods. In: *Summaries of the Third Annual JPL Airborne Geoscience Workshop*, pp. 29–31.
- El-Kazzaz, Y.A.H.A., Taylor, W.E.G., 2001. Tectonic evolution of the Allaqi shear zone and implications for Pan-African terrane amalgamation in the southern Eastern Desert, Egypt. *Journal of African Earth Sciences* 33, 177–197.
- El-Nisr, S.A., 1997. Late Precambrian volcanism at Wadi Allaqi, Southeastern Desert, Egypt: evidence for transitional continental arc/margin environment. *Journal of African Earth Sciences* 24, 301–313.
- Green, A.A., Craig, M.D., 1985. Analysis of aircraft spectrometer data with logarithmic residuals. In: *Proceedings, AIS Workshop*, 8–10 April, 1985, Jet Propulsion Laboratory, Pasadena, California, pp. 111–119.
- Green, A.A., Berman, M., Switzer, P., Craig, M.D., 1988. A transformation for ordering multispectral data in terms of image quality with implications for noise removal. *IEEE Transactions on Geoscience and Remote Sensing* 26, 65–74.
- Jensen, J.R., 2000. *Remote Sensing of the Environment: An Earth Resource Perspective*. Prentice Hall, Upper Saddle River, NJ, p. 544.
- Jensen, J.R., 2005. *Introductory Digital Image Processing*. Person Prentice Hall, Upper Saddle River, p. 526.
- Kruse, F.A., Raines, G.L., Watson, K., 1985. Analytical techniques for extracting geologic information from multichannel airborne spectroradiometer and airborne imaging spectrometer data. In: *Proceedings, International Symposium on Remote Sensing of Environment, Thematic Conference on Remote Sensing for Exploration Geology*, 4th, Environmental Research Institute of Michigan, Ann Arbor, pp. 309–324.
- Kruse, F.A., Lefkoff, A.B., Boardman, J.W., Heidebrecht, K.B., Shapiro, A.T., Barloon, P.J., Goetz, A.F.H., 1993. The Spectral Image Processing System (SIPS) Interactive Visualization and Analysis of Imaging Spectrometer Data. *Remote Sensing of Environment* 44, 145–163.
- Kusky, T.M., Ramadan, T.M., 2002. Structural controls on Neoproterozoic mineralization in the South Eastern Desert, Egypt: an integrated field, Landsat TM, and SIR-C/X-SAR approach. *Journal of African Earth Sciences* 35, 107–121.
- Leica Geosystems, 2003. *ERDAS Field Guide*. Leica GeoSystems, Atlanta, Georgia, p. 672.
- Liu, J.G., Mason, P.J., Clerici, N., Chen, S., Davis, A., Miao, F., Deng, H., Liang, L., 2004. Landslide hazard assessment in the three Gorges area of the Yangtze river using ASTER imagery: Zigui-Badong. *Geomorphology* 61, 171–187.
- NASA ASTER, 2004. *Advanced Spaceborne Thermal Emission and Reflection Radiometer*. Available from: <<http://asterweb.jpl.nasa.gov>>.
- NASA AVIRIS, 2004. *Airborne Visible/Infrared Imaging Spectrometer*. Available from: <<http://aviris.jpl.nasa.gov>>.
- NASA LANDSAT 7, 2004. *Landsat Program Update*. Available from: <http://landsat.gsfc.nasa.gov/main/PDF/program_handouts/program_update_nov04_lr.pdf>.
- NASA MODIS, 2004. *Moderate Resolution Imaging Spectrometer*. Available from: <<http://modis.gsfc.nasa.gov>>.
- Ramadan, T.M., Abdelsalam, M.G., Stern, R.J., 2001. Mapping gold-bearing massive sulfide deposits in the Neoproterozoic Allaqi suture, Southeast Egypt with Landsat TM and SIR-C/X-SAR images. *Photogrammetric Engineering and Remote Sensing* 67, 491–497.
- Research Systems, Inc., 2002. *ENVI Tutorials*. Research Systems, Inc., Boulder, CO, p. 640.
- Rowan, L.C., Mars, J.C., 2003. Lithologic mapping in the Mountain Pass, California area using Advanced Spaceborne Thermal Emission and Reflection Radiometer (ASTER) data. *Remote Sensing of Environment* 84, 350–366.
- Stern, R.J., 1994. Arc assembly and continental collision in the Neoproterozoic East African Orogen: implications for the consideration of Gondwanaland. *Annual Reviews Earth and Planetary Science Letters* 22, 319–351.
- SulSoft Ltda., 2004. *AsterDTM 2.2 Installation & User's Guide*, Porto Alegre/RS, Brazil, p. 38.
- Swayze, G.A., Clark, R.N., 1995. Spectral identification of minerals using imaging spectrometry data: evaluating the effects of signal to noise and spectral resolution using the Tricorder Algorithm. In: *Summaries of the Fifth Annual JPL Airborne Earth Science Workshop*, pp. 157–158.
- Vaughan, R.G., Calvin, W.M., Taranik, J.V., 2003. SEBASS hyperspectral thermal infrared data: surface emissivity measurement and mineral mapping. *Remote Sensing of Environment* 85, 48–63.
- Welch, R., Jordan, T., Lang, H., Murakami, H., 1998. ASTER as a source for topographic data in the late 1990's. *IEEE Transactions on Geoscience and Remote Sensing* 36, 1282–1289.
- Yamaguchi, Y., Fujisada, H., Tsu, H., Sato, I., Watanabe, H., Kato, M., Kudoh, M., Kahle, A.B., Pniel, M., 2001. ASTER early image evaluation. *Advanced Space Research* 28, 69–76.
- Zhang, B., Wang, X., Liu, J., Zheng, L., Tong, Q., 2000. Hyperspectral image processing and analysis system (HIPAS) and its applications. *Photogrammetric Engineering and Remote Sensing* 66, 605–609.